Large-Scale Block Bundle Adjustment of LROC NAC Images for Lunar South Pole Mapping Based on Topographic Constraint

Chen Chen , Zhen Ye , *Member, IEEE*, Yusheng Xu , Dayong Liu , Rong Huang , *Member, IEEE*, Miyu Zhou , Huan Xie , *Senior Member, IEEE*, and Xiaohua Tong , *Senior Member, IEEE*

Abstract—With the increasing interest in the south polar region of the Moon, there is an urgent need for high-resolution mapping products to support future exploration. Bundle block adjustment (BBA) is able to improve the spatial positioning accuracy of images used to generate high-precision mapping products. However, the impacts of weak-convergence geometry and poor illumination conditions in lunar south pole on BBA still need to be solved. This article proposes a large-scale robust BBA method for narrow angle camera (NAC) images in south pole. The NAC images are taken from the Lunar Reconnaissance Orbiter, which are scanner-type images requiring special treatment beyond the classical BBA of framing camera images. To handle the weak-convergence geometry issue of stereo NAC imagery, a topographic constraint using reference digital elevation model is integrated into BBA with an appropriate weighting scheme to estimate local topographic relief. In addition, a two-stage outlier elimination strategy for BBA with absolute-relative thresholding and iteratively reweighting methods is presented to reject outliers caused by the poor illumination conditions in lunar south pole. Thousands of images are used for experimental tests and lunar orbiter laser altimeter digital elevation models (DEMs) with different resolutions are used as reference data. The satisfactory experimental results demonstrate the effectiveness and reliability of our BBA method. The proposed large-scale BBA method reduces the relative positioning errors in block network to within 1 m, and decreases the inconsistency between NAC images caused by the orientation errors to less than 0.5 pixel, which offers a reliable solution for large-scale controlled mapping.

Index Terms—Large-scale bundle block adjustment (BBA), lunar south pole, outlier elimination, topographic constraint, weak convergence.

The authors are with the College of Surveying and Geo-Informatics, Tongji University, Shanghai 200092, Chinaand also with the Shanghai Key Laboratory for Planetary Mapping and Remote Sensing for Deep Space Exploration, Shanghai 200092, China (e-mail: 1911213@tongji.edu.cn; 89_yezhen@tongji.edu.cn; yusheng_xu@tongji.edu.cn; liudy@tongji.edu.cn; rong_huang@tongji.edu.cn; zmy_tj@tongji.edu.cn; huanxie@tongji.edu.cn; xhtong@tongji.edu.cn).

I. INTRODUCTION

DUE to the abundant resources and unique environmental characteristics of lunar south pole, many countries plan to carry out exploration missions, including in-situ science and resource exploration plan of CHANG'E-7 from China [1], the Lunar Polar Exploration mission from India and Japan [2], the Artemis program from United States [3] and the International Lunar Research Station program at the south pole of the Moon [4]. Therefore, it is essential to construct valuable digital elevation models (DEMs) and digital orthophoto maps of lunar south pole to support these exploration missions. However, the measurement errors in spacecraft positions and attitudes give rise to distortions in image mosaic and DEM elevation when constructing large-scale lunar south polar mapping products [5], [6]. In order to diminish these errors, bundle block adjustment (BBA) is necessarily conducted to achieve consistent geometric accuracy of images in the block network. The adjustment solution will be used to correct the navigation data of the involved images, which is an important requirement for the production of gridded digital terrain models (DTMs) and orthoimage mosaics.

Lunar Reconnaissance Orbiter (LRO) carries two narrow angle cameras (NACs, NACL, and NACR) that are capable of providing meter-scale panchromatic images over a 5 km swath from the 50 km orbit. Each camera is equipped with a 700-mm focal-length telescope featuring a 5000-pixel charge coupled device (CCD) line-array, which provides an IFOV of 10 μrad and a cross-track field-of-view of 2.85° [7]. NAC images have been applied in landing site selection, small-scale safety assessment for potential landing sites, and safe guidance and trajectory analysis of landers [8]. Due to varying errors of LRO orbit and attitude measurements, geographical positioning errors will lead to the inconsistency between the calculated position of ground point and actual position corresponding to images [9]. The Lunar Reconnaissance Orbiter Camera (LROC) operations team corrected these geometric errors using the temperature correction on C-matrix kernels [10]. However, south polar images still have offsets up to ∼100 m from their actual positions because of residual errors in C-kernels that had been used [6]. In addition, the unique design of LROC NACs brings difficulties to the BBA of images in lunar south pole. Since off-nadir slewing disrupts nadir measurements by other instruments on the spacecraft, the NACs are typically of nadir direction. This

leads to weak-convergence geometry of NAC images, which refers to the conditions when convergence angles are less than 10° [9]. Large-scale BBA of these NAC images is subjected to the elevation error caused by weak convergence geometry [11]. This elevation error will be more pronounced in lunar south pole, considering the south polar region characterizes a much more rugged terrain. On the other hand, low-quality matching results were often caused by weak image correspondence due to illumination changes, especially the complicated illumination conditions of lunar south pole make the results worse. In this case, the convergence of BBA iteration cannot be guaranteed due to the low-quality image matching.

Regarding to the existing large-scale products in lunar south pole, there are still some problems that need to be further considered in BBA. Wagner et al. [12] generated a polar mosaic covering from 85.5° to the south pole, but clear stitching lines exist in the mosaic. Afterward, they tried their efforts to use the JIGSAW application in integrated software for imagers and spectrometers (ISIS) to conduct a BBA routine on LROC NAC polar images, whereas the BBA results were not well-controlled and not extended to the entire polar dataset with available resources [6]. Therefore, a brute-force automated control method was adopted to align images in 2-D map space [6]. The U.S. Geological Survey Center created a near-global lunar control network using the Kaguya terrain camera (TC) morning stereoscopic and monoscopic datasets. Bundle adjustment was performed using the ISIS JIGSAW application when the shaded version of the LRO Lunar Orbiter Laser Altimeter (LOLA) DEM was used to create control networks [13]. The resolution of mosaic product is 10m/pixel. Meanwhile, they are trying to create geodetically controlled 1 m/pixel lunar south polar cap mosaics with LROC NAC images, poleward from 85° latitude. The BBA was performed with a constraint of LOLA track data [14]. In their work, a NASA Ames application [15] was used to match illuminated LOLA track data to images in order to provide absolute constraints, but the performance of the coregistration is limited by poor quality of the simulated images because of the large sampling interval of the laser altimeter [16]. Moreover, when LOLA points are used as an absolute constraint in BBA, the distribution and quality of the laser points will directly affect the accuracy of the BBA results [17], [18].

Aiming at solving the instability and uncertainty of BBA solutions caused by weak-convergence geometry and low-quality matching, a large-scale robust BBA method for images with weak-convergence geometry is presented in this article. Compared with previous studies, the following components are integrated into BBA processing. First, a topographic constraint method is developed that aims to deal with the weak convergence condition of LROC NACs in south pole. An appropriate weighting scheme is introduced in the topographic constraint to weaken the influence of prior elevation error. Second, to handle the mismatch problem caused by weak texture information of images in south polar region, a two-stage outlier elimination strategy using absolute-relative thresholding and iteratively reweighting method (ARW) is proposed, which is stable even for block network with a lot of outliers caused by poor illumination. The proposed BBA method is performed on thousands of NAC

images, and the overall geometric refinement of NAC images is achieved, which is of great significance for enhancing the geometric accuracy of orthomaps and DEMs generated from NAC images.

The rest of this article is organized as follows. Section II reviews the recent developments on BBA of orbiter imagery. Section III describes the proposed large-scale BBA method. Section IV presents a systematic experimental evaluation of the proposed method using LROC NAC images covering the south polar regions. Section V further analyzes the robustness and limitation of the proposed method. Finally, Section VI concludes this article.

II. RELATED WORKS

This study focuses on large-scale BBA of orbiter images with weak-convergence geometry and poor imaging quality in lunar south pole. The existing works on BBA of planetary orbiter images and processing methods dealing with the issues of weak geometry and outliers in BBA will be briefly reviewed in this section.

A. BBA of Planetary Orbiter Images

When a stereo mapping camera is carried on the orbiter, such as the three-line-array camera of the Chang′e-1 (CE-1) [19], the TDI-CCD stereo camera of the Chang′e-2 (CE-2) [20], and the high-resolution stereo camera of Mars Express [21], the images captured by these cameras can usually be directly adjusted through BBA using their stereo geometric conditions. The main limitations lie in the selection of images with appropriate illumination conditions (e.g., incidence angles and phase angles) [22], the lack of control points [23], and the different stereo geometric configurations of images [24], [25]. For planetary remote sensing imagery, most matching algorithms fail when the images have large differences in illumination and subtle textures. Some studies focused on dealing with these problems and achieved good results [26], [27]. The LROC NAC images have been used to generate featured NAC mosaics [28] and DTM products [29] by the LROC team. Since the LROC NAC were designed not for stereo observation, these products were produced by stereo images at limited coverage areas.

Several researchers have studied the BBA method of LROC NAC images. Li et al. [30] presented a BBA method to improve the accuracy of the EO parameters of NAC stereo images. The polynomial function with scanning time was used to model the EO parameters, and the polynomial coefficients were adjusted iteratively in the BBA. The residual errors have been reduced from dozens of pixels to a subpixel level after performing BBA. Li et al. [31] first performed a boresight calibration between the two NAC cameras, and then, developed a LOLA integrated bundle adjustment combining the LOLA data, tie points (TPs), and six EO parameters. The experimental results show that the positioning accuracy of topographic maps can be significantly improved. Although the tilt angle between NAC-L and NAC-R is small, the two cameras do not share the same lens and, thus, cannot be modeled with a single rigorous camera model. Therefore, both the deviation between two NACs and the deviation between

the camera and orbiter should be corrected [29], [30], [32], [33]. Lin [34] developed a rigorous photogrammetric processing method for LROC NAC images, and separated the estimation of boresight parameters from the traditional BBA. It was concluded that the boresight parameters estimation may not be included in the general BBA of image orientation parameters so as to avoid incorrect solution as a result of the parameteric correlation between the boresight parameters and EO parameters. Unlike the separation of boresight parameters estimation and traditional BBA in [34], Hu and Wu [35] proposed a single combined free-network block adjustment for all four images, which is able to decrease the gaps and inconsistencies caused by the inaccurate boresight offsets between the two NAC cameras and the irregular overlapping regions. However, these methods primarily focus on a small number of images in local areas.

At present, planetary mapping software such as the commercial software SOCET SET [36], the ISIS system [37], and Ames Stereo Pipeline has been adopted in LROC NAC images processing and DEMs generation [38], [39]. In the ISIS JIGSAW application, the position and pointing of LRO NACs could be calculated separately or simultaneously, and the 3-D positions (latitude, longitude, and radius) of all ground points could also be determined. Through weighting on the adjustment parameters, these parameters can be fixed, allowed to be adjusted freely, or constrained by a priori accuracy information [40]. However, the performance of ISIS JIGSAW application is not satisfactory when the TPs contain severe outliers. In addition, SOCET SET produced a general pushbroom sensor model, which can be applied to connect the image space with the object space. The parameters, such as position, speed, and pointing angle, are adjusted to minimize the root mean square (RMS) of residuals between all ground points and TPs by multisensor triangulation [41]. A team from DLR (German Aerospace Center) and TUB (Technical University Berlin) developed a stereo photogrammetric system to process LROC NAC images and to produce 2 m-resolution DEMs of the Apollo 17 landing site [32], [42], and the lunar south pole area for the European Space Agency's (ESA) lunar landing missions [43].

B. BBA of Weak-Convergence Images

As previously mentioned, the existing lunar mapping research works are typically based on a limited number of well-conditioned stereo images through photogrammetric processing. However, the weak convergence geometry of images is inevitable in large-scale BBA. In order to solve this problem, the existing control source, such as DEM, is considered to be added to the BBA properly. The DEM is directly used as an elevational reference [44], [45], [46]. Cheng et al. [47] took the elevation value extracted from the DEM as the observed value with errors, and then, built BBA model combined with the measured image coordinates. In addition, Zhou et al. [48] and Zhang et al. [49] conducted similar studies. Briskin et al. [50] added the constraint of DEM as an additional term to the BBA cost function. The terrain surface is expressed using a second-order function. Cao et al. [51] took the DEM as constraint on the object space coordinates of TPs. However, all these

DEM-aided BBA methods are typically used in Earth orbiter optical images, and few examinations have been conducted to analyze the effectiveness of the BBA of planetary orbiter optical images. The difference between DEM-aided BBA of Earth and planetary images mainly lies in that there are rare ground control points on the planetary surface, so more attention needs to be paid to the weighting strategy of BBA parameters.

C. Outlier Elimination Method Within BBA

The number of TPs obtained by automatic matching is enormous when involving massive images, while there inevitably exist a large number of mismatching TPs regarded as outliers. This issue will directly lead to the deformation of the block network and decrease the reliability of BBA results. Therefore, a robust outlier detection and elimination method is essential.

The outlier elimination methods typically rely on setting a certain threshold value. The statistical values of reprojection residuals are usually used as the relative threshold values, which are determined based on the difference between the measured and calculated image coordinates. For example, Li et al. [52] calculated the residual of each TP during each iteration in the BBA of the HIRIC image in Tianwen-1 landing site. The residuals whose values exceed three times the mean square error (MSE) are considered outliers. Some studies take the TPs with residuals over three times the rms as outliers [53].

In addition, adding a loss function in the objective function of BBA was adopted to reduce the influence of outliers on the solution of nonlinear least squares problems [54]. But strong nonlinearity has been introduced into the objective function by robustification works, which should be considered in the optimization routine of bundle adjustment. In addition, iteratively reweighting is another method of eliminating outliers in observation values by changing the weight of the observation values appropriately [55].

For large-scale block networks, suitable strategies were still needed for detecting and eliminating outliers. Some studies have combined multiple methods to eliminate mismatches, such as the multistage outlier elimination strategy, including outlier detection and outlier rejection [56]. These methods have been well applied to Earth satellite images [57]. However, there are few research works focusing on the robustness of BBA methods for lunar orbiter images, especially when numerous outliers exist in the dataset of south pole environment. In this article, a two-stage outlier elimination strategy in BBA is developed by combining absolute thresholding, relative thresholding, and iteratively reweighting method to reject outliers caused by the poor illumination conditions in lunar south pole.

III. METHODOLOGY

This article proposes a large-scale robust BBA method for LRO NAC images in lunar south pole based on the topographic constraint. The overall workflow of the proposed BBA method is shown in Fig. 1, which includes the establishment of the imaging model, construction of the BBA model with topographic constraint, and outlier elimination. The input of the BBA method is a number of NAC images, which are preprocessed from the
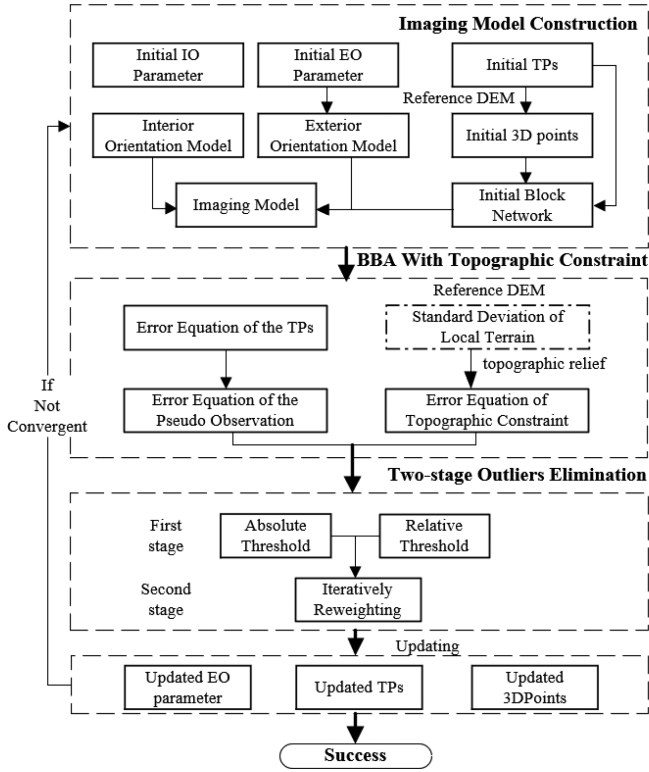
Fig. 1. Overall workflow of the proposed BBA method of weak-convergence NAC images.

original experiment data record using ISIS software [58]. This process eliminates the noise in the NAC images and enhances the images with the initial EO parameters extracted from the SPICE kernel.

The basic model of large-scale BBA for NAC images is established using the observation equation of TPs based on the collinearity equation and the pseudo-observation equation of EO parameters. The following characteristics are included in the proposed method of large-scale BBA processing. To solve the weak-convergence problem, a topographic constraint equation with an appropriate weighting scheme is assisted in the basic BBA model. Considering the influence of prior errors of the reference DEM, the weight of elevation correction value is set by estimating the prior error under different topographic relief. Subsequently, to solve the low matching quality of images in lunar south pole, a two-stage outlier elimination strategy is developed in BBA. The first stage is absolute-relative thresholding, which rejects the outliers by a certain threshold, and the second stage is iteratively reweighting, which reweights residuals based on the results of the previous BBA iteration.

A. Basic Model of Large-Scale BBA Method

The basic function model of BBA is the linearized form of collinearity equation, which specifies the perspective center of camera, the image measurement point, and its corresponding ground point lie on the same observation ray. The relationship between 3-D ground points and the corresponding image points is represented by the following:

$$\begin{bmatrix} X - X_S \\ Y - Y_s \\ Z - Z_s \end{bmatrix} = \lambda R_{\text{MOON\_FIXED}}^{J2000} R_{J2000}^{\text{LRO\_SC\_BUS}} R_{\text{LRO\_SC\_BUS}}^{\text{NACL}/R} \begin{bmatrix} x \\ y \\ f \end{bmatrix}$$

$$= \lambda R \begin{bmatrix} x \\ y \\ f \end{bmatrix} \qquad (1)$$

where $[x, y, f]^T$ is the focal plane coordinate of image point, $[X, Y, Z]^T$ is the ground point coordinate corresponding to image point, $[X_S, Y_S, Z_S]^T$ is the coordinate of LRO in lunar body fixed coordinate system, $R_{\text{LRO\_SC\_BUS}}^{\text{NACLR}}$ is the rotation matrix from NAC camera coordinate system to LRO coordinate system, $R_{J2000}^{\text{LRO\_SC\_BUS}}$ is the rotation matrix from LRO coordinate system to the J2000 coordinate system, $R_{\text{MOON\_FIXED}}^{J2000}$ is the rotation matrix from the J2000 coordinate system to the lunar fixed coordinate system, and λ is the scale factor.

For pushbroom cameras, each scanning line has a specific set of EO parameters, which can be modeled using a polynomial function with imaging time. Second-order polynomials model is applied as the interpolation function for each EO parameter

$$\begin{bmatrix} X_S^{ij} \\ Y_S^{ij} \\ Z_S^{ij} \\ \varphi^{ij} \\ \omega^{ij} \\ \kappa^{ij} \end{bmatrix} = \begin{bmatrix} a_0 & a_1 & a_2 \\ b_0 & b_1 & b_2 \\ c_0 & c_1 & c_2 \\ d_0 & d_1 & d_2 \\ e_0 & e_1 & e_2 \\ f_0 & f_1 & f_2 \end{bmatrix} \begin{bmatrix} 1 \\ t \\ t^2 \end{bmatrix} \qquad (2)$$

where t is the imaging time of the image measurements at (i, j), $a_0, \ldots, f_n$ are the coefficients, $[X_S^{ij}, Y_S^{ij}, Z_S^{ij}]^T$ is the LRO position at time t, $[\varphi^{ij}, \omega^{ij}, \kappa^{ij}]^T$ is the LROC NACs rotation angle at time t, φ is right ascension angles, ω is declination angles, and κ is the angle of camera rotation around the boresight.

In this article, all TPs, ground points, and EO parameters of images are treated as weighted observation values. In particular, the basic error equations of our BBA model include the following three parts:

$$V_1 = AX_1 - L_1, \ P_1$$
$$V_2 = BX_2 - L_2, \ P_2$$
$$V_3 = C_1 X_1 + C_2 X_2 + C_3 X_3 - L_3, \ P_3 \qquad (3)$$

where V_1 and V_2 are the pseudo-observation equations for the position and attitude angles of the orbiter, which are added to appropriately enhance the stability of parameter adjustment, so that the corrected parameters do not excessively deviate from the initial value after adjustment, V_3 is the observation equation of the TPs, the coefficient matrix A, B, and C_i (i = 1, 2, 3) contains partial derivatives with respect to the unknown parameters, X_1, X_2, X_3 are the vector of the orbiter position, the polynomial coefficient of the orbiter attitude angle, and the vector of the unknown ground coordinate of the TPs, L_1, L_2 are the observation vectors of the corresponding EO polynomial parameters, L_3 is the observation vector of the TPs, and P_i (i = 1, 2, 3) are the weight values of equations.

The high-resolution linear array CCD sensor has the characteristics of high flight altitude, narrow imaging beam, and close to parallel projection. As a result, there typically exists a high correlation between the position and attitude parameters, which will lead to the divergence or instability of the solution of BBA equation. In order to deal with these correlations, the weighting strategy of these parameters must be carefully considered. The weights of the position and attitude parameters can be calculated using the prior accuracy of the position and attitude data as

$$P_1 = \frac{1}{\sigma_{\text{pos}}^2}$$

$$P_2 = \frac{1}{\sigma_{\text{ang}}^2}$$

$$P_3 = \frac{1}{\sigma_{\text{TPs}}^2} * W \tag{4}$$

where σ_{pos} and σ_{ang} are the prior accuracy of position and pointing for LROC NACs, which can be set at 1 m and 0.01°. σ_{TPs} is the prior matching accuracy of TPs, W denotes the weight determined by the iteratively weighting method, which will be described in Section III-C.

B. Topographic Constraint Based on Reference DEM for Weak-Convergence Images

Most of NAC images suffer from the problem of weak convergence geometry due to the specific design of the LROC, which makes the elevation calculation unstable and reduces the overall accuracy of BBA in lunar south pole. To solve this problem, a topographic constraint based on reference DEM is introduced to ensure stable estimation of the BBA parameters. The complete mathematical expression of the spatial surface equation corresponding to the DEM is difficult to obtain, and is generally approximated using local fitting. In this article, assuming the expression function of DEM is represented with two variables as follows:

$$z = f(x, y) \tag{5}$$

where z is the elevation of DEM, and (x, y) are the horizontal coordinates, $f(x, y)$ correspond to the expression of DEM at (x, y).

The difference between the DEM and the 3-D points corresponding to the TPs can be minimized as follows:

$$\arg \min \| h_{\text{TPs}} - f_{\text{TPs}}(\text{lat}, \text{lon}) \|_2. \tag{6}$$

where h_{TPs} is the elevation of TPs, and (lat, lon) are the horizontal coordinates of TPs, $f_{\text{TPs}}(\text{lat}, \text{lon})$ correspond to the expression of DEM at latitude and longitude of TPs. The error equation is derived as follows:

$$v = \frac{\partial f(\text{lat}, \text{lon})}{\partial \text{lat}} \Delta \text{lat} + \frac{\partial f(\text{lat}, \text{lon})}{\partial \text{lon}} \Delta \text{lon}$$
$$- \Delta h - (h_0 - f(\text{lat}_0, \text{lon}_0)), \ P_4 \tag{7}$$

where $\frac{\partial f(\text{lat}, \text{lon})}{\partial \text{lat}}$ and $\frac{\partial f(\text{lat}, \text{lon})}{\partial \text{lon}}$ are the slope of DEM in the north–south and east–west directions, $h_{\text{DEM}}(\text{lat}_0, \text{lon}_0)$ is the elevation of the DEM at $(\text{lat}_0, \text{lon}_0)$, $(\text{lat}_0, \text{lon}_0, h_0)$ is the coordinate

of 3-D point, $(\Delta \text{lat}, \Delta \text{lon}, \Delta h)$ is the correction of 3-D point coordinate. The slope of DEM is, then, calculated pixel-by-pixel with a 3×3 sample grid based on Horn's algorithm [59].

Finally, the topographic constraint error equation V_4 based on the (7) can be expressed as follows:

$$V_4 = DX_3 - L_4, \ P_4 \tag{8}$$

where the coefficient matrix D contains partial derivatives with respect to the unknown parameters, X_3 is the vector of the unknown ground coordinate of TPs, L_4 is the coordinate of 3-D point, and P_4 is the weight value of the topographic constraint error equation.

An appropriate weighting scheme is essential to a successful BBA solution. If there is a large prior geographic reference error in DEM, it may lead to an obvious error in the initial altitude of TPs in the area with large topographic relief. The influence of the prior elevation error under different topographic relief can be weakened through reducing the weight of elevation correction in BBA. The weight is determined based on the slope, which is manifested as the larger the local terrain undulation (slope) in the DEM, the smaller the weight. In this article, in order to weaken the influence of prior error of reference DEM, the weight of elevation correction value is set by estimating the prior error of different topographic relief. The mean value D_h of local terrain is calculated as follows:

$$D_h = \frac{\sum_{i=1}^n H_i^P}{n}, \ P \in 11 \times 11 \text{ grid} \tag{9}$$

where H_i^P is the elevation of the ith grid from the reference DEM. Standard deviation σ_h of local terrain is then calculated with D_h as follows:

$$\sigma_h = \sqrt{\frac{\sum_{i=1}^n (H_i^P - D_h)^2}{n}}. \tag{10}$$

For the complicated topography in lunar polar region, especially in the steep slopes and craters, the fitting or interpolation accuracy of elevation varies frequently when constructing DEMs, whereas the changes in lunar mare are relatively gentle. Therefore, the greater the topographic relief, the lower the elevation reliability. The weight P_4 of elevation correction value considering the topographic relief information is set as follows:

$$P_4 = \frac{1}{\sigma_h}. \tag{11}$$

According to (7), the error equation term for a single 3-D ground point is denoted as v_i. The gradient of this term is given by $(\frac{\partial v_i}{\partial \text{lat}}, \frac{\partial v_i}{\partial \text{lon}}, \frac{\partial v_i}{\partial h})_{1 \times 3}$ that relates to a 3-D ground point. The optimization of the BBA is based on the Schur complement trick and Cholesky factorization [60].

C. Two-Stage Outliers Elimination Strategy of TPs

Large-scale block network in BBA often contains a large number of outliers due to weak image correspondence caused by illumination changes, especially for images in lunar south pole with varying illumination conditions. This will seriously decrease the performance of BBA. A threshold of the reprojection residual values can be set based on prior knowledge
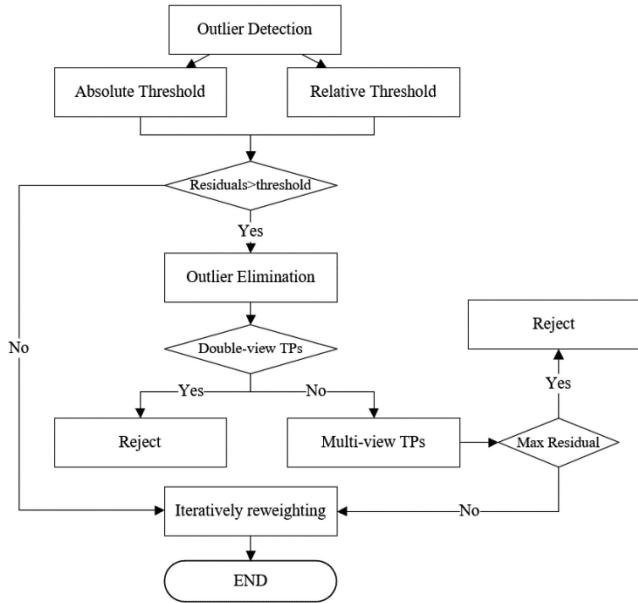
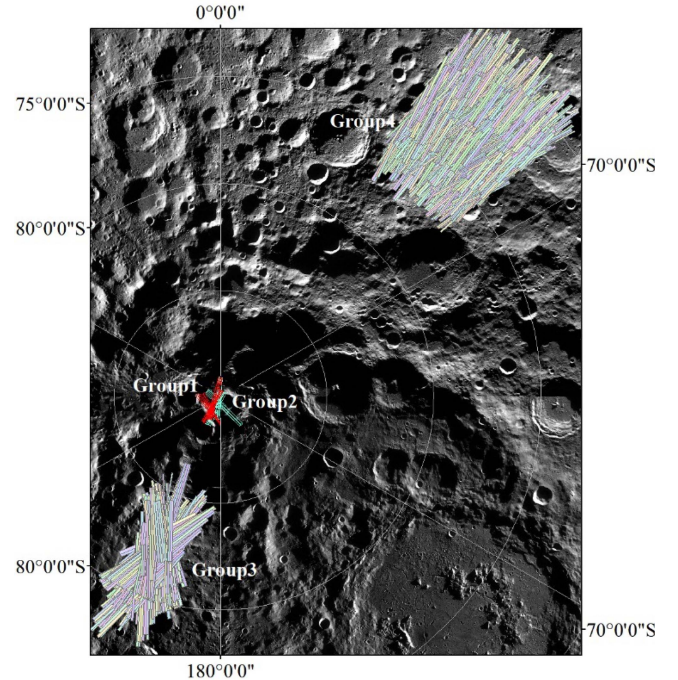Fig. 2.   Proposed two-stage outlier elimination strategy.

Fig. 3.   Overview of the south pole area including the locations of the four experimental areas and LROC NAC footprints of the four areas. (Different colors of image footprints represent footprints of different images. To distinguish footprints between Groups 1 and 2, set the colors to red and cyan, respectively. The base map is the Moon LROC WAC global morphology mosaic provided by NASA [65].)

to find and remove outliers. However, the large-scale block network involves a large number of image TPs, and the TPs corresponding to the same ground point may exist on multiple images. The iteratively reweighting method can reweight the observation values based on the results of the previous iteration. Therefore, a two-stage outlier elimination strategy combining ARW method is proposed to eliminate the mismatching points in the BBA, as shown in Fig. 2.

1) Absolute-Relative Thresholding: In each iteration of BBA, if the residual of a TP exceeds a certain absolute threshold, it will be rejected. For orbiter imagery captured from high altitude, the residual vectors of the TPs without outliers on the same image should have good consistency in terms of magnitude and direction [61]. Therefore, three times rms calculated by all pixels in a single scene image are used as the relative threshold to detect the outliers. When the difference between the residual of a TP and the mean value of residuals is greater than the relative threshold, the TP is considered an outlier [58].

2) Iteratively Reweighting: The iteratively reweighting method uses a slowly growing function instead of the quadratic sum of the residuals to reduce the weight of gross error and attenuate the effect on the BBA result. The remaining small-scale outliers are eliminated through the iteratively reweighting strategy in each iteration. The IGG weighting function [62] is utilized, which is expressed as follows:

$$W_i = \begin{cases} p_i, & |v_i| \leq k_0 \\ p_i \frac{k_0}{|v_i|}, & k_0 < |v_i| \leq k_1 \\ 0, & k_1 < |v_i| \end{cases} \qquad (12)$$

where W_i is the weight of the measurements of the TPs, p_i is the obtained weight for the previous iteration, the initial weight matrix p_0 is the unit matrix, v_i is the reprojection residual of the TPs, and k_0, k_1 are endpoints of the intervals. Generally, take $k_0 = 1.5\sigma$ and $k_1 = 2.5\sigma$, σ is the root MSE of the residuals.

IV. EXPERIMENTAL RESULTS AND ANALYSIS

A. Experimental Details

The images used in experiments were collected from LROC NACs in lunar south pole. To make it easier to obtain high-quality TPs, images with similar resolution and better illumination conditions were selected to validate the performance of BBA processing. Ground sampling distance ratio and delta solar azimuth angle in [63] are used to select images with similar resolution and illumination. The incidence angle is limited within 40°–90°, not 40°–65° in [63], due to the complex illumination conditions in lunar south pole. The other criteria used for finding image candidates with better illumination conditions is calculated by the percentage of illuminated area within the overlapping area of the image pair. A feature matching algorithm for orbiter images was applied to generate accurate TPs automatically [64].

This article sets up four experimental areas in lunar south pole, and Fig. 3 shows an overview of the south pole area including the locations of these experimental areas. The main information of the used experimental data is listed in Table I. Two of the experimental areas are the potential landing sites (connecting ridge and Shackleton crater rim) for ESA Lunar Lander and Artemis III of NASA. The connecting ridge includes 16 images and 15 256 TPs, and the Shackleton Crater Rim includes 14 images and 10 253 TPs. There are no outliers in the TPs of these two groups. The other two large experimental areas contain thousands of images in lunar south pole. Laveran is a lunar

TABLE I
MAIN INFORMATION OF LROC NAC IMAGES USED IN THE EXPERIMENTS

Region	Group Index	Number of Images	Resolution	Number of TPs	Location
Connecting Ridge	1	16	0.93m—1.27m	15 256	89.348°S—89.581°S 209.961°E—234.516°E
Shackleton Crater Rim	2	14	0.95m—1.31m	10 253	89.633°S—89.840°S 180.819°E—226.615°E
Laveran Area	3	1240	1.17m—1.70m	296 598	80.01°S—83.23°S 200.05°E—204.20°E
Boguslawsky Area	4	2541	0.45m—1.29m	453 987	68.12°S—78.01°S 33.71°E—48.82°E

TABLE II
MAIN INFORMATION OF PARAMETERS SOLVED IN THE BBA

Group Index	Number of Double-view TPs	Number of Multi-view TPs	Number of Observables	Number of Unknown Parameters
1	11 322	3934	30 512	21 183
2	10 110	143	20 506	15 540
3	275 808	20 790	593 196	456 042
4	424 324	29 663	907 974	711 483

Fig. 4. Illustration of manners to calculate 3-D ground coordinates. (a) Ray-tracing estimation. (b) Triangulation.

impact crater located on the lunar far side near the southern pole, which is in the third experimental area. Boguslawsky was selected as the primary landing site for the Russian Luna-Glob mission, which is in the fourth experimental area. The Laveran Area includes 1240 images and more than 296 000 TPs, and the Boguslawsky area includes 2541 images and more than 453 000 TPs. There exist a considerable number of outliers in the TPs of these two groups.

The statistical data are added in Table II to show the TPs connecting and the number of observations and unknown parameters to be solved for in the BBA.

The reference DEM used for experiments with images of Groups 1 and 2 is the improved 5 m LOLA DEM for south pole landing sites [66], and the reference DEM used for Groups 3 and 4 is the 30 and 60 m LOLA DEM downloaded from the NASA Planetary Data System.

A primary objective of the proposed large-scale BBA with topographic constraint is to reduce the inconsistency induced by errors in the initial EO parameters of the NAC images. To demonstrate the effectiveness of the proposed method, a series of experiments are conducted based on four groups of datasets. The reprojection residuals, relative positioning errors, elevation deviation and orthomaps are used to evaluate the performance of BBA.

The reprojection residuals in image space are calculated by the difference between the matched image coordinates and the reprojected image coordinates. The relative positioning errors are calculated by the difference of 3-D ground points intersected by the TPs from different image pairs. In order to calculate the relative positioning errors, the 3-D ground coordinates of TPs should be first determined. According to the intersection angle of TPs in the block network, the TPs are divided into two
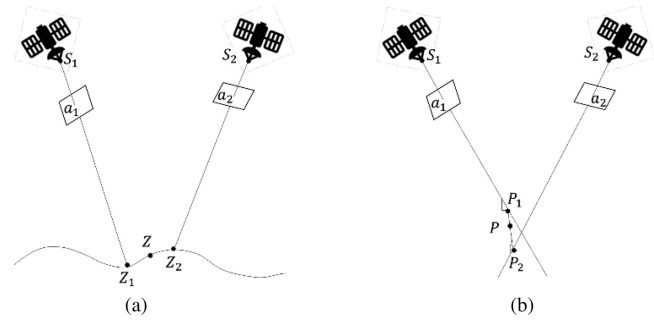
types, i.e., weak intersection TPs (intersection angle $< 10°$) and strong intersection TPs (intersection angle $\geq 10°$). Regarding these two types, various manners are adopted to calculate their corresponding initial 3-D ground coordinates, as shown in Fig. 4.

The calculation manner for weak intersection TPs is using the ray tracing method [67] that obtains two ground positions on the existing DEM and calculates the midpoint of them. Therefore, relative positioning errors of weak intersection TPs can be calculated by the difference between two ground positions obtained from ray tracing with DEM. The calculation manner for the strong intersection TPs is using the triangulation method [68] that the triangulated point is located in the middle of the shortest line segment connecting two rays. There are multiple observation rays for multiview TPs, so that two or more ground positions will be calculated by the triangulation method. The relative positioning errors of strong intersection TPs can finally be calculated by the difference between these calculated ground positions.

Meanwhile, the elevation deviation between the measured 3-D points and DEM, the elevation deviation of DEMs conducted from different stereo image pairs, and the deviation of orthomap mosaic are calculated to analyze the absolute accuracy.

B. Overall Performance of the Proposed BBA Method

In this section, the proposed large-scale BBA method is tested using the images in Groups 3 and 4. The performance of our BBA method is quantitatively evaluated by the reprojection residuals of TPs and the relative positioning errors of images. In addition, the elevation deviation between the measured 3-D points and reference LOLA DEM is calculated to demonstrate the absolute elevation accuracy of the proposed BBA method. These results before BBA are computed by the initial EO parameters of images and initial ground coordinates of TPs, whereas the results after large-scale BBA are computed by the adjusted EO parameters of images and optimized ground coordinates of TPs.

The rms and maximum absolute (Max) value of the reprojection residuals are calculated in both directions. As shown in Table III, the RMS of reprojection residuals before BBA in the sample (cross-track) and line (along-track) directions are both worse than 10 pixels. After performing our BBA method, it is improved to less than 0.5 pixels in two directions. Moreover, the Max value of reprojection residuals is reduced from hundreds

TABLE III
STATISTICS OF REPROJECTION RESIDUALS FOR LARGE-SCALE BBA METHOD

Group Index		RMS (pix)		Max (pix)	
		Sample	Line	Sample	Line
3	Before BBA	11.6605	13.0017	1245.9928	112.9227
	After our BBA	0.4254	0.3977	1.0160	0.9995
4	Before BBA	9.8430	12.3586	1643.9952	410.3917
	After our BBA	0.4225	0.3761	1.7256	1.1986

TABLE IV
STATISTICS OF RELATIVE POSITIONING ERRORS FOR LARGE-SCALE BBA METHOD

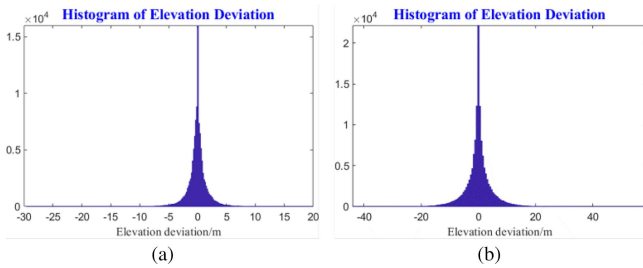| Group Index		X (m)	Y (m)	Z (m)	XYZ (m)
3	Before BBA	10.2595	17.5815	3.3145	20.6241
	After our BBA	0.8323	0.8736	0.7301	1.4103
4	Before BBA	7.7979	9.7808	5.3845	13.6185
	After our BBA	0.4158	0.4116	0.8599	1.0401

Fig. 5.   Histogram of elevation deviation after performing BBA. (a) Results of Group 3. (b) Results of Group 4.

of pixels to within 2 pixels. The RMS in cross-track direction is slightly larger than that in along-track direction after our BBA. The main reason is that elevation changes affect cross-track (sample) reprojection more than along-track (line) due to the intersection angles of TPs in cross-track are obviously larger than those in along-track direction.

Table IV lists the relative positioning errors that are estimated through the ray tracing method of weak intersection TPs in Groups 3 and 4. The relative positioning errors reflect the consistency between 3-D points corresponding to the TPs on different image pairs. Before BBA, there exist obvious systematic relative positioning errors in three directions. The relative positioning errors are reduced to within 1 m in all three directions after performing our BBA method. The total relative positioning errors are less than 1.5 m.

The elevation deviation between the measured 3-D points obtained after BBA and the LOLA DEM are calculated, and the histogram of elevation deviation is shown in Fig. 5. After performing our BBA method, the measured 3-D point should be located on the surface of LOLA DEM. Therefore, the statistical value of the elevation deviation should be relatively small. The mean value and the rms of the elevation deviation are –0.004 and 1.757 m, respectively, in Group 3. In Group 4, the mean value and the rms of the relative elevation deviation are

TABLE V
STATISTICS OF REPROJECTION RESIDUALS FOR DIFFERENT BBA METHODS

Group Index	Method	RMS (pix)		Max (pix)	
		Sample	Line	Sample	Line
1	Before BBA	1.7681	4.6585	7.0472	21.7657
	BBA without topographic constraint	0.3930	0.1867	0.7642	0.7640
	BBA with topographic constraint	0.2456	0.2329	0.5277	0.5280
2	Before BBA	1.9112	0.8648	6.3767	12.6354
	BBA without topographic constraint	0.4567	0.0731	0.7709	0.7567
	BBA with topographic constraint	0.2979	0.2824	0.6304	0.6306

0.011 and 4.606 m, respectively. The possible reason for the larger rms value in Group 4 is the lower resolution of the LOLA DEM.

C. Performance of Topographic Constraint With Reference DEM

To demonstrate the effectiveness of topographic constraint with reference LOLA DEM, the BBA methods without and with the topographic constraint are conducted on images in Groups 1 and 2 for comparison. In addition to the evaluation metrics mentioned in Section IV-B, profiles are drawn on the LOLA DEM and photogrammetric DEMs. Photogrammetric DEMs are generated from image pairs before and after BBA. Subsequently, the elevation derived from the profiles indicates the absolute positioning accuracy of the adjusted EO parameters in BBA. Orthomaps are generated to illustrate the geometric differences of the image pairs.

The reprojection residuals of TPs are exported, and the detailed statistics are summarized in Table V. The rms and Max value of the reprojection residuals are quite large before BBA. After constructing the BBA method without the topographic constraint, the rms in sample direction is smaller than in line direction due to the strong convergence geometry of images. After constructing the BBA method with the topographic constraint, the rms of reprojection residuals is limited to within 0.3 pixel in sample and line directions. Due to the addition of topographic constraint, the rms in line direction of the BBA with topographic constraint method is slightly larger than that of the BBA method without the topographic constraint. In plane direction, the results of BBA with topographic constraint method outperform the BBA method without the constraint.

The relative positioning errors are calculated by triangulating 3-D points from the strong intersection TPs in Groups 1 and 2. The statistical values of relative positioning errors are shown in Table VI. Before BBA, obvious systematic errors can be found in Z direction. After BBA without the constraint of DEM, the relative positioning errors are reduced to about 1.5 m in all three directions. After BBA with topographic constraint, the relative positioning errors are reduced to less than 1 m in all three directions.

TABLE VI
STATISTICS OF RELATIVE POSITIONING ERRORS FOR DIFFERENT BBA
METHODS

Group Index	Method	X (m)	Y (m)	Z (m)	XYZ (m)
1	Before BBA	3.2830	1.1257	15.4042	15.7903
	BBA without topographic constraint	0.2360	0.1438	0.7812	0.8286
	BBA with topographic constraint	0.2161	0.1421	0.7153	0.7606
2	Before BBA	0.4011	0.5328	13.4532	13.4697
	BBA without topographic constraint	0.3733	0.0843	1.1678	1.2289
	BBA with topographic constraint	0.1804	0.1826	0.8661	0.9033
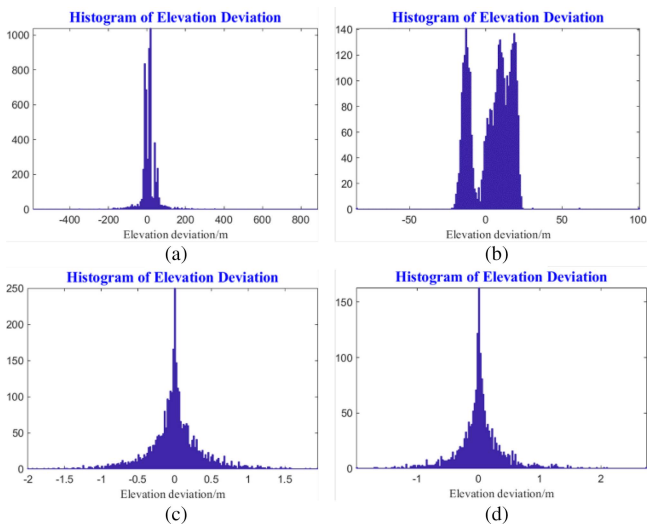
Fig. 6. Histogram of Elevation Deviation. (a) Results of Group 1 after BBA without topographic constraint. (b) Results of Group 2 after BBA without topographic constraint. (c) Results of Group 1 after BBA with topographic constraint. (d) Results of Group 2 after BBA with topographic constraint.

The elevation of 3-D points after BBA is compared with the LOLA DEM in Groups 1 and 2. The histogram of elevation deviation after BBA is shown in Fig. 6. After BBA without the constraint of LOLA DEM, the mean value and the rms of the elevation deviation are 8.400 and 44.642 m in Group 1, and are 4.244 m and 12.641 m in Group 2, as shown in Fig. 6(a) and (b). The lack of DEM control in BBA results in large elevation deviation. After BBA with the topographic constraint, the mean value and the rms of the elevation deviation are –0.003 and 0.313 m in Group 1, as shown in Fig. 6(c). In Group 2, the mean value and the rms of the elevation deviation are –0.003 and 0.461 m, as shown in Fig. 6(d). The distribution of elevation deviation follows a normal distribution with the aid of the topographic constraint.

To further assess the performance, the elevation deviation of different DEMs is displayed. DEMs with a resolution of 2 m/pixel were derived from the selected image pairs in Groups 1 and 2, as shown in Fig. 7(a) and (d), and the reference 5 m/pixel LOLA DEM was used for comparison. The generated DEMs and profiles drawn on DEMs are given in Fig. 7(b), (c), and (e). The elevation of the profiles on DEMs generated before and after BBA is shown in Fig. 8. The results of profile comparisons reemphasize that the elevation values of DEMs generated from the images after BBA are close to the elevation values of reference LOLA DEM. The local areas are enlarged and displayed in Fig. 8(b) and (d). There exists a small deviation between the elevation of these profiles. The possible explanations for these differences could be as follows:

1) the details revealed in photogrammetric DEM are missed by the 5 m LOLA DEM because of the resolution difference;
2) remained errors are contained in the LOLA DEM after processing of laser points; and
3) small misregistration still exists between the generated DEM and the LOLA DEM.

In order to compare the elevation between DEMs generated from different image pairs in the same region, three images were selected in Group 1. The elevation of profiles shown in Fig. 8(b) illustrates a satisfied consistency. Furthermore, the absolute lateral positioning of the images compared with LOLA DEM is able to be reflected by the profiles. It can be inferred that the lateral positioning of the images is consistent with LOLA DEM.

To demonstrate the improvement of geometry consistency between images, the deviation of orthomap mosaics is analyzed. Four image pairs were selected in Groups 1 and 2, respectively. Image pairs were orthorectified and sampled to orthomaps, and craters were used as features for comparison. Figs. 9 and 10 illustrate a qualitative validation by visually comparing the deviations of the plane position of the orthomaps generated using the images before and after our BBA. In each image pair of Figs. 9 and 10, the two left images are orthomaps before BBA, and the two right images are orthomaps after BBA. It can be seen that orthomap mosaics generated before BBA present obvious geometric differences, which are almost completely corrected after performing the BBA with topographic constraint.

D. Performance of Two-Stage Outlier Elimination Strategy

To assess the performance of the proposed two-stage outlier elimination strategy, ARW, two outlier elimination methods are adopted in BBA for comparison. The first method is of ISIS 6.0 JIGSAW application, and the second is the absolute-relative threshold (AR) method. The reprojection residuals of TPs are estimated to demonstrate the effect of the outlier elimination method within BBA, and the vectors of reprojection residuals before and after BBA are displayed, respectively, to reflect the BBA results.

Experiments were conducted using images of Groups 1 and 4. The detailed statistics of reprojection residuals before and after BBA are summarized in Tables VII and VIII. When little outlier exists in the block network of Group 1, the ISIS JIGSAW application achieves decent results, but once there exist outliers in the block network of Group 4, the results of the ISIS JIGSAW application are not satisfactory. After BBA with the AR method, there is a significant reduction in the residuals of TPs. In addition, it is obvious that the residuals of TPs after BBA with the ARW strategy are smaller than the results of BBA with other two outlier
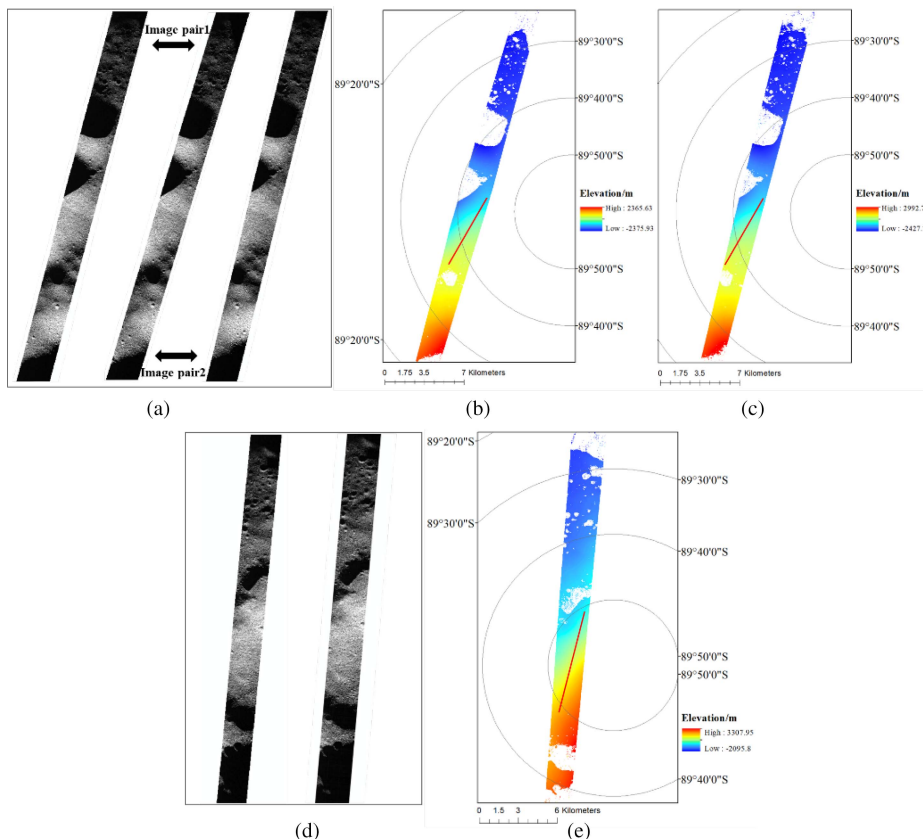
Fig. 7. Images and DEMs results after BBA with topographic constraint. (a) Image pairs in Group 1. (b) DEM generated by Image Pair1 of (a). (c) DEM generated by Image Pair 2 of (a). (d) Image pairs in Group 2. (e) DEM generated by images of (d). Red lines are profile lines on DEMs.
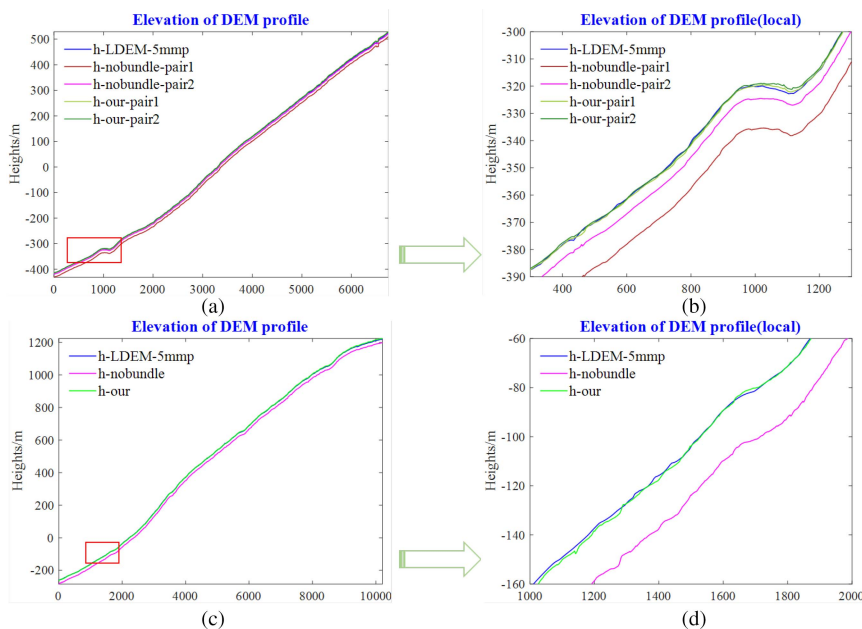

Fig. 8. Profiles comparison of the red line marked in Fig. 7. (a) and (b) are the profiles in Group 1. (c) and (d) are the profiles in Group 2. Different colors correspond to different DEM profiles. Profiles in red boxes of left figure are enlarged and shown in right figure.
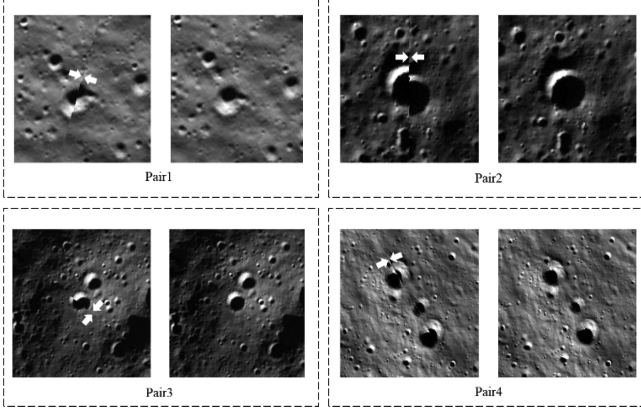
Fig. 9. Orthomaps generated with images before and after BBA with topographic constraint in Group 1. In each image pair, the left orthomap mosaic is generated before BBA, and the right orthomap mosaic is generated after BBA. (White arrow points to the splicing line.)
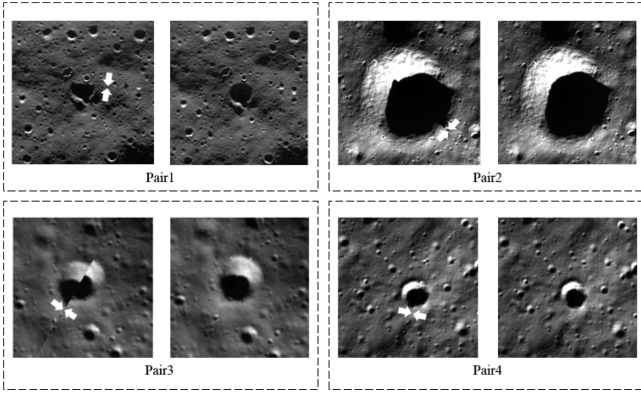

Fig. 10. Orthomaps generated with images before and after BBA with topographic constraint in Group 2. In each image pair, the left orthomap mosaic is generated before BBA, and the right orthomap mosaic is generated after BBA. (White arrow points to the splicing line.)

TABLE VII
STATISTICS OF REPROJECTION RESIDUALS FOR BBA WITH DIFFERENT
OUTLIER ELIMINATION METHODS

Group Index	Method	RMS (pix)		Max (pix)	
		Sample	Line	Sample	Line
1	Before BBA	1.7681	4.6585	7.0472	21.7657
	ISIS 6.0	0.7525	0.2599	3.3984	2.0702
	BBA with AR	0.4116	0.2155	0.9975	0.9972
	BBA with ARW	0.3930	0.1867	0.7642	0.7640

TABLE VIII
STATISTICS OF REPROJECTION RESIDUALS FOR BBA WITH DIFFERENT
OUTLIER ELIMINATION METHODS

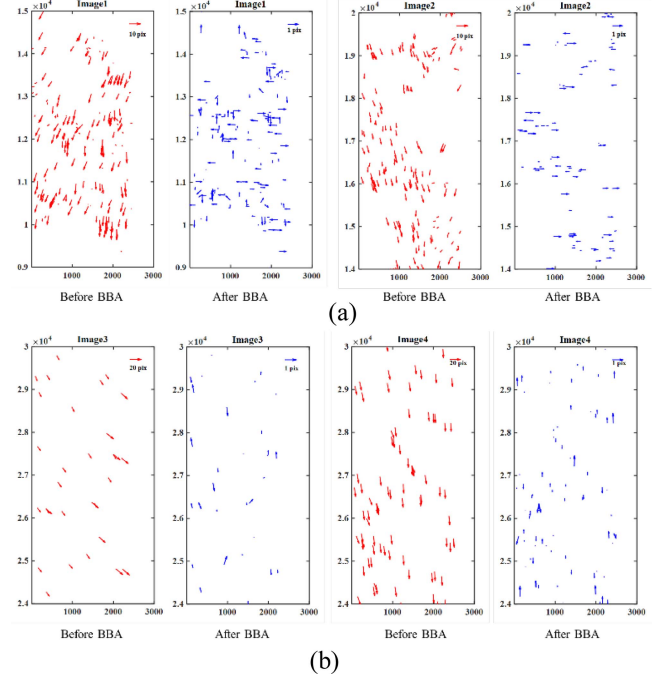| Group Index	Method	RMS (pix)		Max (pix)	
		Sample	Line	Sample	Line
4	Before BBA	9.8471	12.3586	1643.5652	410.2939
	ISIS 6.0	0.1444	0.7019	15.0784	79.6831
	BBA with AR	0.1507	0.5408	1.9860	1.9998
	BBA with ARW	0.1395	0.4950	1.8676	1.8670

Fig. 11. Distribution of reprojection residuals before and after BBA with ARW. (a) Results of Group 1. (b) Results of Group 4. Scales of reprojection residuals of TPs before BBA are ten or twenty times larger than after BBA.

elimination methods. The rms of the residuals after BBA with ARW is limited to about 0.5 pixel.

Two images were selected, respectively, in Groups 1 and 4, and the residual vectors before and after BBA with ARW are illustrated in Fig. 11. Before BBA, the magnitudes and directions of the residual vectors are relatively consistent, which indicates obvious systematic errors appear in the residuals of the TPs. After BBA with ARW, the smaller magnitudes and random directions of the residual vectors mean that these systematic errors are almost reduced. The reprojection residuals of TPs are reduced from about ten or twenty pixels before BBA to less than a pixel after BBA with ARW, which demonstrates the effect of the proposed outlier elimination strategy. As shown in Fig. 11, the reprojection residuals of Group 1 in cross-track direction are larger than in along-track direction after BBA, while the reprojection residuals of Group 4 in along-track direction are larger than in cross-track direction. The main reason is that the TPs in Group 1 have strong intersection geometry, and the errors in along-track direction can be readily reduced without the topographic constraint. However, without the topographic constraint, errors in the along-track direction are difficult to reduced significantly owing to the weak convergence of images in Group 4.

E. Independent Assessment of the Proposed BBA Method

To assess the performance of the proposed BBA method independently, 4335 and 1460 independent checkpoints (CPs) were additionally matched in Groups 1 and 2. The performance is quantitatively evaluated by the reprojection residuals and the relative positioning errors of these CPs.

TABLE IX
STATISTICS OF REPROJECTION RESIDUALS FOR BBA WITH CPS

Group Index		RMS (pix)		Max (pix)	
1	Before BBA	1.0738	2.1762	6.3103	11.1323
	After BBA	0.6059	0.3236	5.1745	2.3931
2	Before BBA	0.9285	1.1371	5.5446	10.0839
	After BBA	0.5992	0.1877	4.5695	2.5854

TABLE X
STATISTICS OF RELATIVE POSITIONING ERRORS FOR BBA WITH CPS

Group Index		X (m)	Y (m)	Z (m)
1	Before BBA	2.9594	1.1106	15.0358
	After BBA	0.4922	0.3771	1.9666
2	Before BBA	0.3024	0.3899	17.2745
	After BBA	0.1925	0.4582	2.0145

TABLE XI
STATISTICS OF RELATIVE POSITIONING ERRORS FOR BBA WITH DIFFERENT DEMs

Group Index	BBA With Different DEMs	X (m)	Y (m)	Z (m)	XYZ (m)
1	Before BBA	2.9594	1.1106	15.0358	15.3645
	BBA with 5 m LOLA DEM	0.4922	0.3771	1.9666	2.0620
	BBA with 20 m CE-2 DEM	0.4793	0.3810	1.8390	1.9382
	BBA with 20 m LOLA DEM	0.4900	0.3770	2.0470	2.1383
	BBA with 60 m LOLA DEM	0.5332	0.5166	3.0467	3.1358
2	Before BBA	0.3024	0.3899	17.2745	17.2815
	BBA with 5 m LOLA DEM	0.1925	0.4582	2.0145	2.0749
	BBA with 20 m CE-2 DEM	0.1746	0.4832	1.9069	1.9749
	BBA with 20 m LOLA DEM	0.1630	0.4830	1.8407	1.9100
	BBA with 60 m LOLA DEM	0.2331	0.4907	3.5222	3.5638

TABLE XII
STATISTICS OF ELEVATION DEVIATION FOR BBA WITH DIFFERENT DEMs

Group Index	BBA With Different DEMs	Mean (m)	RMS (m)
1	Before BBA	1.7157	10.3669
	BBA with 5 m LOLA DEM	-0.2078	2.2952
	BBA with 20 m CE-2 DEM	-0.1217	2.7546
	BBA with 20 m LOLA DEM	-0.2338	3.2511
	BBA with 60 m LOLA DEM	-0.4548	6.9164
2	Before BBA	6.5261	14.2935
	BBA with 5 m LOLA DEM	-0.0932	2.6685
	BBA with 20 m CE-2 DEM	0.2283	3.8271
	BBA with 20 m LOLA DEM	0.0710	3.8017
	BBA with 60 m LOLA DEM	1.2681	9.5131

The reprojection residuals of the CPs in the across-track and along-track directions are listed in Table IX. After BBA, the rms of residuals are reduced to about 0.6 pixel. The statistics of relative positioning errors are listed in Table X. After BBA, the relative positioning errors are approximately 2 m in both groups. The results demonstrate that the proposed BBA method can reduce the relative positioning errors of LROC NAC images in lunar south pole.

V. DISCUSSION

To analyze the robustness of the topographic constraint method to the resolution and noise of reference DEM, two sets of experiments were performed to further discuss the performance of the proposed method.

A. Influence of DEMs With Different Resolutions and From Different Sources

To evaluate the influence of DEMs with different resolutions on the proposed topographic constraint, BBA experiments were conducted separately using different DEMs, namely,

1) 5 m LOLA DEM;
2) 20 m Chang'E-2 (CE-2) DEM [69];
3) 20 m LOLA DEM; and
4) 60 m LOLA DEM.

The BBA results are evaluated by the CPs in Section V-E. The relative positioning errors and the elevation deviation are calculated in Groups 1 and 2. The relative positioning errors in three directions are shown in Table XI, and the mean error and rms of the elevation deviation are shown in Table XII. Furthermore, sample image pairs in Groups 1 and 2 were orthorectified to provide a qualitative comparison in Fig. 12.

With the use of the proposed BBA method, the systematic errors can be effectively reduced. The final accuracy of the BBA method is related to the resolution of reference DEM. It can be seen from the results that the overall effect of BBA degrades with the decreasing of DEM resolution. When the DEM resolution is 60 m, the decrease in accuracy is more significant. Although
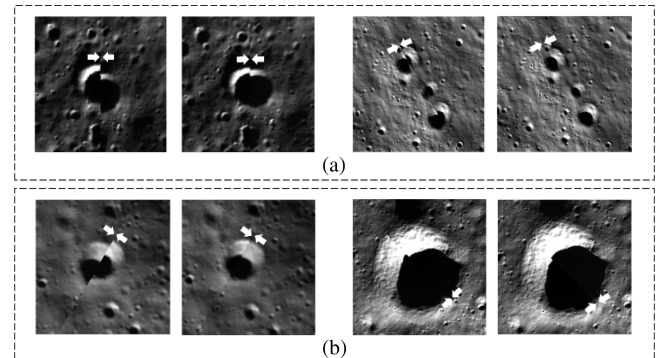

Fig. 12. Orthomaps generated with images before and after BBA in (a) Group 1 and (b) Group 2. In each image pair, the left orthomap mosaic is generated before BBA, and the right orthomap mosaic is generated after BBA using 60 m LOLA DEM. (White arrow points to the splicing line.) (a) Pairs in Group1 (b) Pairs in Group2.

the systematic errors have been effectively reduced using the proposed BBA method, there are still slight offsets between the orthomaps after BBA using the 60 m LOLA DEM as shown in Fig. 12. A possible reason is that low-resolution DEM loses a lot of terrain details, resulting in high-resolution images not being able to correspond to DEM in local areas. In addition, in
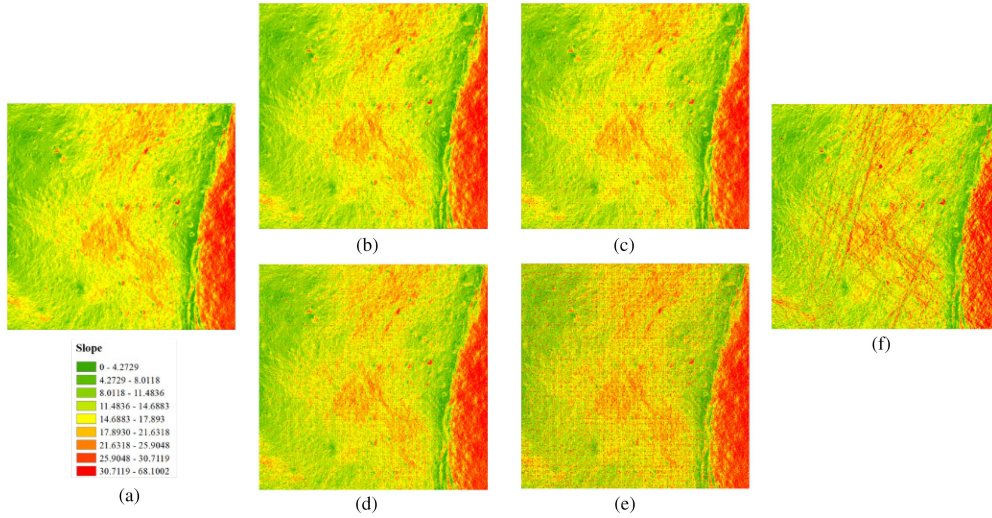
Fig. 13. Slope map of 5 m LOLA DEM with different GNs. (a) 5 m LOLA DEM. (b) GN with $\mu = 0$, $\sigma = 5$ added in 55 m interval. (c) GN with $\mu = 0$, $\sigma = 10$ added in 55 m interval. (d) GN with $\mu = 0$, $\sigma = 5$ added in 25 m interval. (e) GN with $\mu = 0$, $\sigma = 10$ added in 25 m interval. (f) Old 5 m LOLA DEM. (a) 5 m LOLA DEM (b) GN(0,5), 55 m interval (c) GN(0,10), 55 m interval (d) GN(0,5), 25 m interval (e)GN(0,10), 25 m interval (f) Old 5 m LOLA DEM.

TABLE XIII
STATISTICS OF RELATIVE POSITIONING ERRORS FOR BBA USING DEMs WITH DIFFERENT NOISES

Group Index	BBA Using DEMs With Different Noises	X (m)	Y (m)	Z (m)	XYZ (m)
	Before BBA	2.9594	1.1106	15.0358	15.3645
	BBA with 5 m LOLA DEM	0.4922	0.3771	1.9666	2.0620
	BBA with DEM add GN (0,5) 55 m interval	0.4782	0.3744	1.9366	2.0296
1	BBA with DEM add GN (0,10) 55 m interval	0.4783	0.3737	1.9356	2.0285
	BBA with DEM add GN (0,5) 25 m interval	0.4774	0.3717	1.9614	2.0526
	BBA with DEM add GN (0,10) 25 m interval	0.4723	0.3744	1.8716	1.9663
	BBA with old 5 m LOLA DEM	0.4751	0.3712	1.8545	1.9500
	Before BBA	0.3024	0.3899	17.2745	17.2815
	BBA with 5 m LOLA DEM	0.1925	0.4582	2.0145	2.0749
	BBA with DEM add GN (0,5) 55 m interval	0.2361	0.4228	1.9706	2.0292
2	BBA with DEM add GN (0,10) 55 m interval	0.2434	0.4260	2.0025	2.0617
	BBA with DEM add GN (0,5) 25 m interval	0.2424	0.4595	2.0851	2.1489
	BBA with DEM add GN (0,10) 25 m interval	0.2409	0.4095	2.1145	2.1673
	BBA with old 5 m LOLA DEM	0.2284	0.4613	2.0928	2.1552

terms of the results of DEM from different sources, e.g., 20 m CE-2 DEM and 20 m LOLA DEM, the discrepancy on relative positioning accuracy is insignificant.

B. Robustness of the Topographic Constraint

In order to assess the robustness of the proposed topographic constraint to the quality of DEM, varying degrees of Gaussian noise (GN) were added to the 5 m LOLA DEM for conducting BBA. Furthermore, the BBA results with initial release of 5 m LOLA DEM, which described in [66] as "old 5 m/pix LDEM," was also used for comparison. The relative positioning errors after BBA and the elevation deviation between 3-D points and LOLA DEM for CPs were calculated for analyzing the BBA results.

In this experiment, the GN is added to the elevation of the 5 m LOLA DEM for Groups 1 and 2. In order to reflect the varying degrees of noise, the GN with mean $\mu = 0$ m and standard deviation $\sigma = 5$ m and 10 m is added with 25 and 55 m intervals,

TABLE XIV
STATISTICS OF ELEVATION DEVIATION FOR BBA USING DEMs WITH DIFFERENT NOISES

Group Index	BBA Using DEMs With Different Noises	Mean (m)	RMS (m)
	Before BBA	1.7157	10.3669
	BBA with 5 m LOLA DEM	−0.2078	2.2952
	BBA with DEM adding GN (0,5) 55 m interval	−0.1668	2.5272
1	BBA with DEM adding GN (0,10) 55 m interval	−0.1664	2.5075
	BBA with DEM adding GN (0,5) 25 m interval	−0.2009	2.4619
	BBA with DEM adding GN (0,10) 25 m interval	−0.1693	2.3620
	BBA with old 5 m LOLA DEM	0.0458	2.3653
	Before BBA	6.5261	14.2935
	BBA with 5 m LOLA DEM	−0.0932	2.6685
	BBA with DEM adding GN (0,5) 55 m interval	−0.0389	2.7121
2	BBA with DEM adding GN (0,10) 55 m interval	−0.0200	2.7208
	BBA with DEM adding GN (0,5) 25 m interval	−0.0499	2.7241
	BBA with DEM adding GN (0,10) 25 m interval	−0.0618	2.7229
	BBA with old 5 m LOLA DEM	0.1558	2.7313

respectively. Slope maps were constructed from the 5 m LOLA DEM before and after adding noise, as shown in Fig. 13.

The relative positioning errors after BBA are shown in Table XIII. After BBA, the relative positioning errors are reduced within 2.5 m in both experiment groups. The results in Groups 1 and 2 show that using DEM with GN for BBA achieves similar results. The elevation deviation between ground points corresponding to the CPs and DEM before and after BBA is shown in Table XIV. The results show that there is little difference in elevation deviation after BBA. This indicates that the proposed topographic constraint in BBA is robust for using DEMs with different quality.

VI. Conclusion

BBA is an essential step in remote sensing image processing, which can provide high-precision geometric models for subsequent production of surveying and mapping products. In this article, a large-scale BBA method is presented for LROC NAC images in lunar south pole. To solve the problem of weak convergence geometry of LROC NAC images, a topographic constraint based on reference DEM is developed. To deal with mismatching problem caused by the complex illumination conditions of lunar south pole, a two-stage outlier elimination strategy is presented by combining ARW method. Thousands of images in lunar south pole were used to demonstrate the performance of the proposed BBA method.

Through experimental analysis, reasonable consistency among lunar south polar images is achieved via the proposed large-scale BBA method with topographic constraint, resulting in subpixel image residuals and submeter relative positioning errors. The mean value of elevation deviation between the photogrammetric DEMs generated from images after BBA and the reference LOLA DEM is approximately 0.1 m, which demonstrates the effectiveness of the topographic constraint with DEM. The orthomap mosaics illustrate the improvement of geometry consistency between images after DEM-constrained BBA. The rms values of the reprojection residuals are reduced to 0.5 pixel and outperforms the other two compared outlier elimination methods, which reflects the reliability of the proposed two-stage strategy. Furthermore, the robustness of the topographic constraint was analyzed using DEM with different resolutions and quality. The BBA results of DEM with varying noises are close to the DEM without adding errors. However, it must be mentioned that the resolution of DEM affects the accuracy of BBA. The decreasing DEM resolution will deteriorate the BBA performance, but still play a good role in adjusting EO parameters, especially in terms of relative positioning errors.

In future, the DEM-constrained BBA method will be further explored and applied to large-scale processing of more planetary images, and the convergence speed of iteration will be improved.

Acknowledgment

References

[1] Y. Zou, Y. Liu, and Y. Jia, "Overview of China's upcoming CHANG'E series and the scientific objectives and payloads for CHANG'E-7 mission," in *Proc. 51st Lunar Planet. Sci. Conf.*, 2020, p. 1755.

[2] M. Ohtake et al., "Current status of the planned lunar polar exploration mission jointly studied by India and Japan," in *Proc. 52nd Lunar Planet. Sci. Conf.*, 2021, p. 1840.

[3] M. E. Evans and L. D. Graham, "A flexible lunar architecture for exploration (FLARE) supporting NASA's Artemis program," *Acta Astronautica*, vol. 177, pp. 351–372, Dec. 2020, doi: 10.1016/j.actaastro.2020.07.032.

[4] H. Zhang et al., "Overview of lunar exploration and International Lunar Research Station," *Chin. Sci. Bull.*, vol. 65, pp. 2577–2586, Aug. 2020, doi: 10.1360/TB-2020-0582.

[5] E. Mazarico, G. A. Neumann, M. K. Barker, S. Goossens, D. E. Smith, and M. T. Zuber, "Orbit determination of the Lunar Reconnaissance Orbiter: Status after seven years," *Planet. Space Sci.*, vol. 162, pp. 2–19, Nov. 2018, doi: 10.1016/j.pss.2017.10.004.

[6] Z. Ye et al., "Estimation and analysis of along-track attitude jitter of ZiYuan-3 satellite based on relative residuals of tri-band multispectral imagery," *ISPRS J. Photogrammetry Remote Sens.*, vol. 158, pp. 188–200, 2019, doi: 10.1016/j.isprsjprs.2019.10.012.

[7] M. S. Robinson et al., "Lunar Reconnaissance Orbiter camera (LROC) instrument overview," *Space Sci. Rev.*, vol. 150, no. 1–4, pp. 81–124, Jan. 2010, doi: 10.1007/s11214-010-9634-2.

[8] A. A. Kokhanov, I. P. Karachevtseva, A. E. Zubarev, V. Patraty, Z. F. Rodionova, and J. Oberst, "Mapping of potential lunar landing areas using LRO and SELENE data," *Planet. Space Sci.*, vol. 162, pp. 179–189, Nov. 2018, doi: 10.1016/j.pss.2017.08.002.

[9] B. Liu, M. Jia, K. Di, J. Oberst, B. Xu, and W. Wan, "Geopositioning precision analysis of multiple image triangulation using LROC NAC lunar images," *Planet. Space Sci.*, vol. 162, pp. 20–30, 2018, doi: 10.1016/j.pss.2017.07.016.

[10] E. J. Speyerer et al., "Pre-flight and on-orbit geometric calibration of the lunar reconnaissance orbiter camera," *Space Sci. Rev.*, vol. 200, no. 1–4, pp. 357–392, Apr. 2016, doi: 10.1007/s11214-014-0073-3.

[11] Y. Pi, B. Yang, X. Li, and M. Wang, "Robust correction of relative geometric errors among GaoFen-7 regional stereo images based on posteriori compensation," *IEEE J. Sel. Topics Appl. Earth Observ. Remote Sens.*, vol. 15, pp. 3224–3234, 2022, doi: 10.1109/JSTARS.2022.3169474.

[12] R. V. Wagner, E. J. Speyerer, and M. S. Robinson, and the LROC Science Team, "New mosaicked data products from the LROC team," in *Proc. 46th Lunar Planet. Sci. Conf.*, 2015, p. 1473.

[13] L. R. Ostrach, L. A. Weller, and B. H. Wheeler, "Creation of a near-global lunar control network using Kaguya terrain camera data, progress report," in *Proc. 54th Lunar Planet. Sci. Conf.*, 2023, p. 2735.

[14] B. Archinal et al., "Controlled high-resolution LROC NAC Polar mosaics," in *Proc. 54th Lunar Planet. Sci. Conf.*, 2023, p. 2333.

[15] A. V. Nefian, B. Coltin, and T. Fong. "Apollo metric imagery registration to Lunar Orbiter Laser Altimetry," in *Proc. 45th Annu. Lunar Planet. Sci. Conf.*, 2014, p. 1679.

[16] X. Xin, B. Liu, K. Di, M. Jia, and J. Oberst, "High-precision co-registration of orbiter imagery and digital elevation model constrained by both geometric and photometric information," *ISPRS J. Photogrammetry Remote Sens.*, vol. 144, pp. 28–37, 2018, doi: 10.1016/j.isprsjprs.2018.06.016.

[17] G. Li, X. Tang, X. Gao, H. Wang, and Y. Wang, "ZY-3 block adjustment supported by GLAS laser altimetry data," *Photogrammetric Rec.*, vol. 31, no. 153, pp. 88–107, 2016, doi: 10.1111/phor.12138.

[18] H. Xie et al., "Using laser altimetry to finely map the permanently shadowed regions of the Lunar South Pole Using an iterative self-constrained adjustment strategy," *IEEE J. Sel. Topics Appl. Earth Observ. Remote Sens.*, vol. 15, pp. 9796–9808, 2022, doi: 10.1109/JSTARS.2022.3204765.

[19] C. Li, J. Liu, L. Mu, X. Ren, and W. Zuo, "Introduction of the CCD stereo camera," in *The Chang'E-1 Topographic Atlas of the Moon*. Berlin, Germany: Springer, 2016, pp. 1–1.

[20] B. Zhao et al., "Overall scheme and on-orbit images of Chang'E-2 lunar satellite CCD stereo camera," *Sci. China-Technological Sci.*, vol. 54, no. 9, pp. 2237–2242, Sep. 2011, doi: 10.1007/s11431-011-4519-5.

[21] G. Neukum, R. Jaumann, and the HRSC Co-Investigator and Experiment Team, "HRSC: The high resolution stereo camera of Mars Express," in *Mars Express: The Scientific Payload*. Noordwijk, The Netherlands: ESA, pp. 17–35, 2004.

[22] X. Geng, Q. Xu, J. Wang, C. Lan, F. Qin, and S. Xing, "Generation of large-scale orthophoto mosaics using MEX HRSC images for the candidate landing regions of China's first Mars mission," *IEEE Trans. Geosci. Remote Sens.*, vol. 60, 2022, Art. no. 5613520, doi: 10.1109/TGRS.2021.3128518.

[23] Q. Fu et al., "GPU-accelerated PCG method for the block adjustment of large-scale high-resolution optical satellite imagery without GCPs," *Photogrammetric Eng. Remote Sens.*, vol. 89, pp. 211–220, 2023, doi: 10.14358/PERS.22-00051R2.

[24] M. Peng, K. Di, Z. Liu, S. Gou, W. Wan, and Y. Wang, "Topographic mapping capability analysis of moderate resolution imaging camera (MoRIC) imagery of Tianwen-1 Mars mission," *J. Remote Sens.*, vol. 3, 2023, Art. no. 40, doi: 10.34133/remotesensing.0040.

[25] X. Ren et al., "A global adjustment method for photogrammetric processing of Chang'E-2 stereo images," *IEEE Trans. Geosci. Remote Sens.*, vol. 57, no. 9, pp. 6832–6843, Sep. 2019, doi: 10.1109/tgrs.2019.2908813.

[26] B. Wu, H. Zeng, and H. Hu, "Illumination invariant feature point matching for high-resolution planetary remote sensing images," *Planet. Space Sci.*, vol. 152, pp. 45–54, 2018, doi: 10.1016/j.pss.2018.01.007.

[27] W. Yang, Y. Yao, Y. Zhang, and Y. Wan, "Weak texture remote sensing image matching based on hybrid domain features and adaptive description method," *Photogrammetric Rec.*, early assess, p. 26, 2023.

[28] S. M. Klem, M. R. Henriksen, J. Stopar, A. Boyd, M. S. Robinson, and the LROC Science Team, "Controlled LROC narrow angle camera high resolution mosaics," in *Proc. 45th Lunar Planet. Sci. Conf.*, 2014, Art. no. 2885. [Online]. Available: https://ui.adsabs.harvard.edu/abs/2014LPI....45.2885K

[29] T. Tran et al. and the LROC Science Team, "Generating digital terrain models using LROC NAC images," in *Proc. Spec. Joint Symp. ISPRS Tech. Commiss. IV AutoCarto Conjunction ASPRS/CaGIS Fall Spec. Conf.*, vol. 38, 2010, pp. 1–7.

[30] R. Li et al., "Precision photogrammetric modeling of LROC NAC cameras and topographic products," in *Proc. Annu. Meet. Lunar Exploration Anal. Group*, 2010, p. 36.

[31] R. Li et al., "Latest results of 3D topographic mapping using lunar reconnaissance orbiter narrow-angle camera data," in *Proc. 42nd Lunar Planet. Sci. Conf.*, 2011, p. 2010.

[32] J. Oberst et al., "Apollo 17 landing site topography from LROC NAC stereo data - first analysis and results," in *Proc. 41st Lunar Planet. Sci. Conf.*, 2010, p. 2051.

[33] B. Wu and W. C. Liu, "Calibration of boresight offset of LROC NAC imagery for precision lunar topographic mapping," *ISPRS J. Photogrammetry Remote Sens.*, vol. 128, pp. 372–387, 2017, doi: 10.1016/j.isprsjprs.2017.04.012.

[34] L. Lin, "Refined geometric processing of LROC NAC stereo imagery based on the rigorous sensor model," Doctoral dissertation, The Ohio State Univ., Columbus, OH, 2012.

[35] H. Hu and B. Wu, "Block adjustment and coupled epipolar rectification of LROC NAC images for precision lunar topographic mapping," *Planet. Space Sci.*, vol. 160, pp. 26–38, 2018, doi: 10.1016/j.pss.2018.03.002.

[36] A. Walker and A. Pietrzak, "Remote measurement methods for 3-D modeling purposes using BAE Systems' Software," *Geodesy Cartogr.*, vol. 64, pp. 112–124, Jun. 2015, doi: 10.1515/geocart-2015-0009.

[37] J. Anderson, S. Sides, D. Soltész, T. Sucharski, and K. Becker, "Modernization of the integrated software for imagers and spectrometers," in *Proc. Lunar Planet. Sci. Conf.*, vol. 35, 2004, p. 2039.

[38] K. N. Burns, E. J. Speyerer, M. S. Robinson, T. Tran, M. R. Rosiek, and B. A. Archinal, E. H.-Kraus, and the LROC Science Team, "Digital elevation models and derived products from LROC NAC stereo observations," in *Proc. 22nd Congr. Int.-Soc.-for-Photogrammetry–Remote-Sens.*, 2012, pp. 483–488.

[39] J. Laura, D. Miller, and M. Paul, "AMES stereo pipeline derived DEM accuracy experiment using LROC-NAC stereopairs and weighted spatial dependence simulation for lunar site selection," in *Proc. 43rd Lunar Planet. Sci. Conf.*, 2012, Art. no. 2371.

[40] K. Edmundson, D. Cook, O. Thomas, B. Archinal, and R. Kirk, "Jigsaw: The ISIS3 bundle adjustment for extraterrestrial photogrammetry," *ISPRS Ann. Photogrammetry, Remote Sens. Spatial Inf. Sci.*, vol. I-4, pp. 203–208, Jul. 2012, doi: 10.5194/isprsannals-I-4-203-2012.

[41] M. R. Henriksen et al., "Extracting accurate and precise topography from LROC narrow angle camera stereo observations," *Icarus*, vol. 283, pp. 122–137, Feb. 2017, doi: 10.1016/j.icarus.2016.05.012.

[42] I. Haase et al., "Mapping the Apollo 17 landing site area based on Lunar Reconnaissance Orbiter Camera images and Apollo surface photography," *J. Geophysical Res., Planets*, vol. 117, 2012, Art. no. E12.

[43] DLR, "Shackleton Crater rim potential landing site for ESA Lunar Lander DTM." Accessed: Aug. 2, 2023. [Online]. Available: https://wms.lroc.asu.edu/lroc/view_rdr/NAC_DTM_ESALL_SR12

[44] T. A. Teo, L. C. Chen, C. L. Liu, Y. C. Tung, and W. Y. Wu, "DEM-aided block adjustment for satellite images with weak convergence geometry," *IEEE Trans. Geosci. Remote Sens.*, vol. 48, no. 4, pp. 1907–1918, Apr. 2010, doi: 10.1109/tgrs.2009.2033935.

[45] K. Di et al., "High-resolution large-area digital orthophoto map generation using LROC NAC images," *Photogrammetric Eng. Remote Sens.*, vol. 85, pp. 481–491, Jul. 2019, doi: 10.14358/PERS.85.7.481.

[46] X. Zhao, Q. Zhou, J. Dong, and Y. Duan, "Digital elevation model-assisted aerial triangulation method on an unmanned aerial vehicle sweeping camera system," *Photogrammetric Rec.*, vol. 37, no. 178, pp. 208–227, 2022, doi: 10.1111/phor.12419.

[47] C. Cheng, J. Zhang, and G. Huang, "RFM-based block adjustment for spaceborne images with weak convergent geometry," *ISPRS - Int. Arch. Photogrammetry, Remote Sens. Spatial Inf. Sci.*, vol. XL-7/W4, pp. 1–6, Jun. 2015, doi: 10.5194/isprsarchives-XL-7-W4-1-2015.

[48] P. Zhou, X. Tang, N. Cao, X. Wang, G. Li, and H. Zhang, "SRTM-aided stereo image block adjustment without ground control points," *Acta Geodetica et Cartographica Sinica*, vol. 45, no. 11, pp. 1318–1327, 2016.

[49] Y. Zhang, Y. Wan, X. Huang, and X. Ling, "DEM-assisted RFM block adjustment of Pushbroom Nadir viewing HRS imagery," *IEEE Trans. Geosci. Remote Sens.*, vol. 54, no. 2, pp. 1025–1034, Feb. 2016, doi: 10.1109/tgrs.2015.2472498.

[50] G. Briskin, A. Geva, E. Rivlin, and H. Rotstein, "Estimating pose and motion using bundle adjustment and digital elevation model constraints," *IEEE Trans. Aerosp. Electron. Syst.*, vol. 53, no. 4, pp. 1614–1624, Aug. 2017, doi: 10.1109/taes.2017.2667819.

[51] H. Cao, P. Tao, H. Li, and J. Shi, "Bundle adjustment of satellite images based on an equivalent geometric sensor model with digital elevation model," *ISPRS J. Photogrammetry Remote Sens.*, vol. 156, pp. 169–183, Oct. 2019, doi: 10.1016/j.isprsjprs.2019.08.011.

[52] Z. Li et al., "Photogrammetric processing of Tianwen-1 HiRIC imagery for precision topographic mapping on Mars," *IEEE Trans. Geosci. Remote Sens.*, vol. 60, 2022, Art. no. 4601916, doi: 10.1109/TGRS.2022.3194081.

[53] H. Pan, T. Huang, P. Zhou, and Z. Cui, "Self-calibration dense bundle adjustment of multi-view Worldview-3 basic images," *ISPRS J. Photogrammetry Remote Sens.*, vol. 176, pp. 127–138, Jun. 2021, doi: 10.1016/j.isprsjprs.2021.04.013.

[54] M. Cao, S. Li, W. Jia, S. Li, and X. Liu, "Robust bundle adjustment for large-scale structure from motion," *Multimedia Tools Appl.*, vol. 76, no. 21, pp. 21843–21867, Nov. 2017, doi: 10.1007/s11042-017-4581-5.

[55] J. Lu, Y. Chen, B. Li, and X. Fang, "Robust Total Least Squares with reweighting iteration for three-dimensional similarity transformation," *Surv. Rev.*, vol. 46, no. 334, pp. 28–36, 2014.

[56] M. Wang, B. Yang, D. Li, J. Gong, and Y. Pi, "Technologies and applications of block adjustment without control for ZY-3 images covering China," *Geomatics Inf. Sci. Wuhan Univ.*, vol. 42, no. 4, pp. 427–433, 2017.

[57] X. Tong et al., "Optimal selection of virtual control points with planar constraints for large-scale block adjustment of satellite imagery," *Photogrammetric Rec.*, vol. 35, no. 172, pp. 487–508, 2020, doi: 10.1111/phor.12339.

[58] LROC Team, "Working with Lunar Reconnaissance Orbiter LROC narrow angle camera (NAC) data." Accessed: Jul. 10, 2023. [Online]. Available: https://www.lroc.asu.edu/files/DOCS/LROC_NAC_Processing_Guide.pdf

[59] B. K. P. Horn, "Hill shading and the reflectance map," *Proc. IEEE*, vol. 69, no. 1, pp. 14–47, 1981, doi: 10.1109/PROC.1981.11918.

[60] Y. Chen, T. A. Davis, W. W. Hager, and S. Rajamanickam, "Algorithm 887: CHOLMOD, supernodal sparse Cholesky factorization and update/downdate," *ACM T Math Softw.*, vol. 35, no. 3, pp. 1–14, 2008.

[61] B. Wu, H. Hu, and J. Guo, "Integration of Chang'E-2 imagery and LRO laser altimeter data with a combined block adjustment for precision lunar topographic modeling," *Earth Planet. Sci. Lett.*, vol. 391, pp. 1–15, 2014, doi: 10.1016/j.epsl.2014.01.023.

[62] X. Gong and Z. Li, "Robust weighted total least squares based on IGG weighting function," *Acta Geodaetica et Cartographica Sinica*, vol. 43, no. 9, pp. 888–894, 2014.

[63] K. J. Becker et al., "Criteria for automated identification of stereo image pairs," in *Proc. 46th Annu. Lunar Planet. Sci. Conf.*, 2015, no. 1832, Art. no. 2703.

[64] V. R. Jakkula, "Efficient feature detection using OBAloG: Optimized box approximation of Laplacian of Gaussian," Ph.D. dissertation, Dept. Elect. Comput. Eng., Kansas State Univ., Kansas, USA, 2010.

[65] E. Speyerer, M. Robinson, and B. Denevi, "Lunar Reconnaissance Orbiter camera global morphological map of the moon," in *Proc. 42nd Lunar Planet. Sci. Conf.*, 2011, p. 2387.

[66] M. K. Barker, E. Mazarico, G. A. Neumann, D. E. Smith, M. T. Zuber, and J. W. Head, "Improved LOLA elevation maps for south pole landing sites: Error estimates and their impact on illumination conditions," *Planet. Space Sci.*, vol. 203, Sep. 2021, Art. no. 105119, doi: 10.1016/j.pss.2020.105119.

[67] L. Chen and L. H. Lee, "Rigorous generation of digital orthophotos from SPOT images," *Photogrammetric Eng. Remote Sens.*, vol. 59, no. 5, pp. 655–661, May 1993.

[68] G. Slabaugh, R. Schafer, and M. Livingston, "Optimal ray intersection for computing 3D points from n-view correspondences," Deliverable Report, London, pp. 1–11, Feb. 2002.

[69] C. L. Li et al., "Lunar global high-precision terrain reconstruction based on Chang'e-2 stereo images," *Geomatics Inf. Sci. Wuhan Univ.*, vol. 43, no. 4, pp. 485–495, 2018, doi: 10.13203/j.whugis20170400.

Rong Huang (Member, IEEE) received the Ph.D. degree in photogrammetry and remote sensing from Technical University of Munich, Munich, Germany, in 2021.

From 2021 to 2022, she was a Postdoctoral Research Fellow with the Hong Kong Polytechnic University, Hong Kong, China. She is currently an Assistant Professor with the College of Surveying and Geoinformatics, Tongji University, Shanghai, China. Her research interests include photogrammetry and remote sensing, point cloud processing, and 3-D mapping.

Chen Chen received the B.S. degree in surveying and mapping engineering from China University of Petroleum (East China), Qingdao, China, in 2019. She is currently working toward the Ph.D. degree in surveying and mapping science and technology with the College of Surveying and Geoinformatics, Tongji University, Shanghai, China.

Her research interests include photogrammetry, planetary satellite image processing and 3-D mapping.

Miyu Zhou received the B.S. degree in geographic information science from Capital Normal University, Beijing, China, in 2020. She is currently working toward the Ph.D. degree in photogrammetry and remote sensing from Tongji University, Shanghai, China.

Her research interests include photogrammetry, remote sensing, and planetary 3-D mapping.

Zhen Ye (Member, IEEE) received the Ph.D. degree in cartography and geoinformation from Tongji University, Shanghai, China, in 2018.

From 2018 to 2020, he was a Postdoctoral Researcher with the Chair of Photogrammetry and Remote Sensing, Technical University of Munich, Munich, Germany. He is currently an Associate Professor with the College of Surveying and Geoinformatics, Tongji University. His research interests include photogrammetry and remote sensing, high-resolution satellite image processing, and planetary 3-D mapping.

Huan Xie (Senior Member, IEEE) received the B.S. degree in surveying engineering and the M.S. and Ph.D. degrees in cartography and geoinformation from Tongji University, Shanghai, China, in 2003, 2006, and 2009, respectively.

From 2007 to 2008, she was a Visiting Scholar with the Institute of Photogrammetry and Geoinformation, Leibniz Universität Hannover, Hannover, Germany. She is currently a Professor with the College of Surveying and Geo-Informatics, Tongji University. Her research interests include satellite laser altimetry and hyperspectral remote sensing.

Yusheng Xu was born in 1989. He received the B.S. and M.E. degrees in surveying and mapping from Tongji University, Shanghai, China, in 2011 and 2014, respectively, and the Ph.D. and Dr.-Ing. (*summa cum laude*) degrees in photogrammetry and the habilitation (*venia legendi*) in point cloud analysis from the Technical University of Munich (TUM), Munich, Germany, in 2019 and 2022, respectively.

From 2019 to 2022, he was a Lecturer with TUM, Munich, Germany. Since 2022, he joined Tongji University as a Full Professor. He has authored and coauthored more than 40 entries. His research interests include 3-D point cloud processing, image processing, and spaceborne photogrammetry.

Xiaohua Tong (Senior Member, IEEE) received the Ph.D. degree in geographic information system from Tongji University, Shanghai, China in 1999.

Between 2001 and 2003, he was a Postdoctoral Researcher with the State Key Laboratory of Information Engineering in Surveying, Mapping, and Remote Sensing, Wuhan University, Wuhan, China. He was a Research Fellow with Hong Kong Polytechnic University, Hong Kong, in 2006, and a Visiting Scholar with the University of California, Santa Barbara, CA, USA, between 2008 and 2009. He is currently a Professor with the College of Surveying and Geoinformatics, Tongji University. His research interests include remote sensing, geographic information system, uncertainty and spatial data quality, and image processing for high-resolution and hyperspectral images.

Dayong Liu received the B.E. degree in surveying and mapping engineering from China University of Mining and Technology, Xuzhou, China, in 2017. He is currently working toward the Ph.D. degree with the College of Surveying and Geoinformatics, Tongji University, Shanghai, China.

His research interests include photogrammetry and planetary 3-D mapping.